

Succession of resonances to achieve internal wave turbulence

Géraldine Davis¹, Timothée Jamin¹, Julie Deleuze¹, Sylvain Joubaud^{1,2}, Thierry Dauxois¹

1. Univ Lyon, ENS de Lyon, Univ Claude Bernard,
CNRS, Laboratoire de Physique, Lyon, France

2. Institut Universitaire de France (IUF)

(Dated: April 28, 2020)

We study experimentally the interaction of nonlinear internal waves in a stratified fluid confined in a trapezoidal tank. The set-up has been designed to produce internal wave turbulence from monochromatic and polychromatic forcing through three processes. The first is a linear transfer in wavelength obtained by wave reflection on inclined slopes, leading to an internal wave attractor which has a broad wavenumber spectrum. Second is the broad banded time-frequency spectrum of the trapezoidal geometry, as shown by the impulse response of the system. The third one is a nonlinear transfer in frequencies and wavevectors via triadic interactions, which results at large forcing amplitudes in a power law decay of the wavenumber power spectrum. This first experimental spectrum of internal wave turbulence displays a k^{-3} behavior.

Internal gravity waves propagate within density stratified fluids moving under the influence of buoyancy forces [1]. Recently, they have been actively studied in particular because of their importance to mixing and transport in the ocean. For example, a coordinated observational campaign has been performed in the South China Sea [2], which is well-known to contain breaking internal waves with amplitudes up to 200 m. Their generation through the interaction between tides and bathymetry [3], their propagation and instability [4], and their interaction with oceanic currents are just some of the outstanding dynamics being observed. In particular, the study of mixing by breaking internal waves is relevant for the understanding of biological processes such as the vertical redistribution of zooplankton from the deep ocean [5] and the regeneration of the coral reef of Dongsha atoll [6].

In the nonlinear regime, stratified fluid systems may develop turbulence simultaneously due to waves and vortices [7]. Describing the coexistence of each process is a challenge in itself. If stratified turbulence has been actively studied (see [8] and references therein), wave turbulence for internal waves is a relatively unexplored phenomenon. Wave turbulence describes physical systems with a large number of dispersive and nonlinear interacting waves [9] and has been applied to gravity [10], capillary [11] and inertial waves [13], as well as waves in magnetised fluids [12] and in elastic plates [14]. New applications have recently emerged in condensed matter (superfluid Helium and Bose-Einstein condensates), in nonlinear optics [15] and, most recently, in the study of gravitational waves in the early universe [16]. Internal waves are distinct from these waves [17], owing to their unusual dispersion relation. In this letter, we present an experimental set-up that allows us to observe efficient nonlinear energy transfers in frequency and wavenumber and so determine the signature of internal wave turbulence.

The experimental set-up, sketched in Fig. 1(a), is a

confined trapezoidal domain filled with a linear stratified fluid of density $\rho(z)$, in which z is the vertical coordinate. Introducing the gravity g and a reference density ρ_{ref} , the strength of the stratification is characterized by the buoyancy frequency $N = \sqrt{-(g/\rho_{\text{ref}})\partial\rho/\partial z}$. In all the experiments, this is of the order 1 rad/s. The energy is injected at large scale by means of a vertical boundary oscillating horizontally around its mid horizontal axis, with a half cosine shape $a(t) \cos(\pi z/H)$, in which $a(t)$ is the maximum horizontal displacement and H is the depth. The volume is thus kept constant. The classical experiments are performed with a quasi-monochromatic forcing, $a(t) = a_0 \sin(\omega t)$. Here, we also examine impulsive and polychromatic forcings. The resulting velocity fields are measured using the classical particle image velocimetry (PIV) method.

The dispersion relation of internal waves, $\omega = N \sin |\theta|$, is such that the frequency ω sets the angle θ of propa-

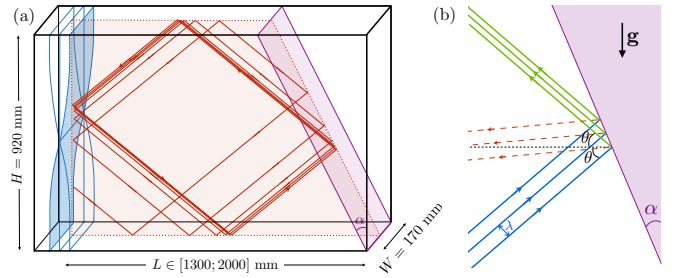


FIG. 1: a) Experimental set-up with the generator on the left of the tank and a slope inclined with an angle α on the right. An example of ray tracing from a single point located on the left hand wall and corresponding to an oscillation at a given frequency $\omega = \pm N \sin \theta$ is shown in the case of a linearly stratified fluid with constant N -value. b) Schematic reflection on a slope of an incident internal gravity beam (in blue) with two wavelengths λ in the transversal direction. The reflected beam does not follow the Snell-Descartes prediction (in dashed red) but keeps the same angle with respect to the horizontal, or with the gravity \mathbf{g} , as shown by the green beam.

gation of internal wave beams and also the ratio of the horizontal to vertical wavenumber. Reflections of internal waves on vertical or horizontal walls are analogous to optical reflection, preserving the angle with respect to the normal of the boundary. On the contrary, reflection on a slope interestingly leads to a ray with the same angle with the horizontal as the incident ray (in absolute value); this is a simple consequence of the preservation of the frequency ω after reflection with the dispersion relation. Figure 1(b) shows that this simple mechanism is even more interesting when considering a beam since both its width and its wavelength are reduced after reflection (notice that, for internal waves, the wavevector is orthogonal to the ray). As the group velocity is proportional to the wavelength, energy conservation leads to efficient energy focusing of the beam.

After multiple reflections, internal waves generated at a given frequency concentrate on a closed loop [18], as illustrated by a single ray traced in Fig. 1(a). The shape and rotational direction of the so-called internal wave attractor (IWA) are independent of the initial emitting point and thus of the spatial structure of the forcing. The IWA can be seen as a limit cycle, a prominent word in nonlinear physics, which arises from linear theory. Different angles of propagation set by different forcing frequencies lead to different attractors with simple or more complicated shapes: the dashed lines in Figure 2(a-f) presents a few (m, n) theoretical attractors, with m reflections on the top and n reflections on the slope.

Due to viscosity, IWAs have finite width as a consequence of the balance between focusing and dissipation as shown in Fig. 2(a-f) [20, 21]. The energy concentration, which is large just after focusing upon reflection from the slope, is progressively dissipated along the length of the attractor before being focused again by the slope. Recent experiments of IWA in two nontrivial three-dimensional set-ups [19] have additionally shown that this is more than a beautiful mathematical curiosity.

It is important to emphasize that this energy focusing with corresponding transfer to small scales arises from linear theory. This is the first important ingredient in the context of wave turbulence as it increases the number of waves with different wavenumbers in interaction.

Owing to energy focusing, the reflected beam has a larger amplitude and is therefore more prone to reach the threshold for triadic resonant instability (TRI) [4, 22]: a beam with primary frequency ω and wavevector \mathbf{k} can excite from background noise two subharmonic waves with frequencies ω_{\pm} and wavevectors \mathbf{k}_{\pm} , satisfying the temporal and spatial resonance conditions $\omega = \omega_{+} + \omega_{-}$ and $\mathbf{k} = \mathbf{k}_{+} + \mathbf{k}_{-}$. Any subharmonic may also become unstable through TRI and/or interact with another pre-existing wave to generate a third one, the latter process being without any amplitude threshold. One thus obtains a necessary ingredient for wave turbulence: a physical mechanism providing multiple nonlinear interactions

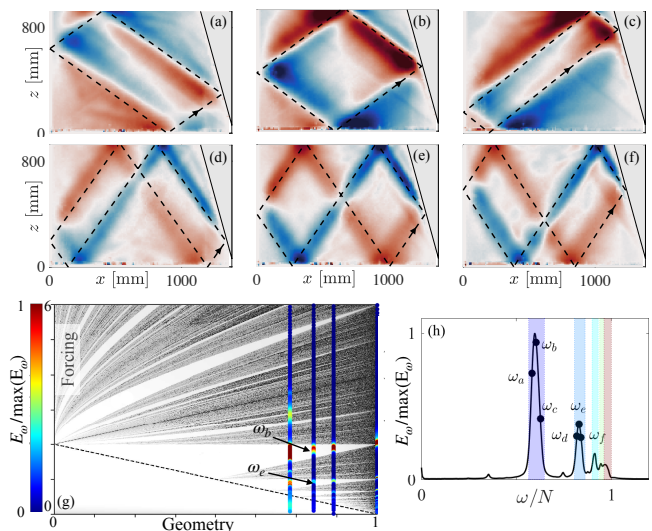


FIG. 2: a-f) Spatial patterns obtained after an initial impulsive kick when the experimental signal is filtered around different frequencies shown with symbols in (h). One recovers (1,1) attractors (a to c) and (2,1) attractors (d to f). The theoretically expected attractors for the geometry and corresponding frequencies are depicted with the dashed line. g) In grey scale, Lyapunov exponents of the trapezoidal domain in the inviscid limit (from [23]) as a function of the geometry $(1 - (2H/L) \tan \alpha)$ and of the forcing $((2H/L) \sqrt{(N/\omega)^2 - 1})$ which is decreasing while increasing the frequency. White regions correspond to strongly convergent attractors. h) Energy spectrum measured experimentally via PIV after an initial kick of the generator for $\alpha = 15.5^\circ$. Vertical colored bands emphasize the theoretical frequency bands of internal wave attractors in the stationary regime. The same spectra for $\alpha = 0, 11.1, 15.5$ and 21.4° are superimposed on (f) as colored vertical lines, from right to left (corresponding graphs are presented in the Supplemental Material [24])

between waves of various wavelengths and frequencies.

The kicked attractor experiment. Before building on this method to achieve internal wave turbulence, we consider the special case of transient impulsive forcing by analogy with musicians striking a tuning fork that resonates at a specific constant pitch.

If the internal wave generator is set into motion with time-dependent amplitude $a(t)$, which is non-zero in a short interval $\delta t \ll 2\pi/N$, then a broad frequency spectrum will be simultaneously excited. We then consider the impulse response of the trapezoidal domain.

Besides, plotting the Lyapunov exponent quantifies the exponential divergence of rays issued from close initial points. Figure 2(g) presents the theoretical prediction [23] in the inviscid limit. White tongues correspond to domains of existence of the different (m, n) attractors.

The impulse response of the different experiments are analyzed by considering the frequency content of the kinetic energy $E_\omega(\omega) = \int (|\tilde{u}(x, z, \omega)|^2 + |\tilde{w}(x, z, \omega)|^2) dx dz$, computed from

the Fourier transform of the two components of the velocity field and integrated over (x, z) plane. Such energy spectra probe complete vertical lines in Fig. 2(g). In the absence of any inclined slope ($\alpha = 0$), when the geometry is 1 in Fig. 2(g), one gets a set of well-peaked discrete modes as shown by the rightmost vertical line (see the energy spectrum in the Supplemental Material [24]). This is expected because attractors, which require a sloping boundary, cannot exist in a rectangular domain. One thus recovers the discrete set of resonance frequencies of the rectangle. The width of these peaks observed experimentally is due to viscous effects. On the contrary, for non-zero α , Fig. 2(g) shows that discrete modes are replaced by vertical bands located within the domain of existence of the different IWAs. These bands of peak energy are plotted in Fig. 2(h) for a given geometry. Filtering the velocity field at given frequencies allows us to disentangle the different responses to the initial impulsive kick. Figures 2(a-f) present different attractors that appear when the signal is filtered around frequencies belonging to the (1,1) and (2,1) tongues of Fig. 2(a). Note that only IWAs with short perimeters (*i.e.* with small m and n values) are visible in presence of damping.

Introducing a slope therefore modifies the usual picture of a wave operator with discrete eigenmodes to some continuous spectrum, and understanding the linear response of these systems is a non-trivial question [25]. By taking advantage of such frequency band within one of the tongue we can efficiently force the system in a polychromatic way, thus increasing the number of waves in interaction. As almost all regions of the physical domain will be covered by an IWA, this characteristic also allows us to inject energy rather homogeneously. Both properties are beneficial in the study of wave turbulence.

Beyond the linear regime. We first consider the transition to nonlinear dynamics resulting from monochromatic forcing $a(t) = a_0 \sin(\omega_0 t)$. Inspired by the transition to wave turbulence observed numerically in harmonically forced elastic plates [26], the amplitude of the generator a_0 is gradually (from 2 to 10 mm) and slowly (over 750 oscillating periods) increased, as shown in Fig. 3(a). The frequency has been chosen within the (1, 1) tongue. The velocity field, whose horizontal component is presented in Fig. 3(b-d) at three different times, is analyzed with the time-frequency function, $S_{\mathbf{u}}(t, \omega) = \langle | \int_{-\infty}^{+\infty} dt' h(t-t') e^{i\omega t'} u |^2 + | \int_{-\infty}^{+\infty} dt' h(t-t') e^{i\omega t'} w |^2 \rangle_{x,z}$, which is plotted in Fig. 3(e). The function h is a hanning window of $80 T_0$. This time window is wide enough to resolve subharmonic frequencies and narrow enough to consider forcing amplitude constant within its duration (increase of 0.85 mm). The horizontal dark-red line at $\omega/N = 0.62$ in Fig. 3(e) corresponds to the forcing frequency. One distinguishes several different regimes: the *linear regime* (Fig. 3(b)) with a monochromatic response leading to a well-defined single attractor. Figure 3(c) cor-

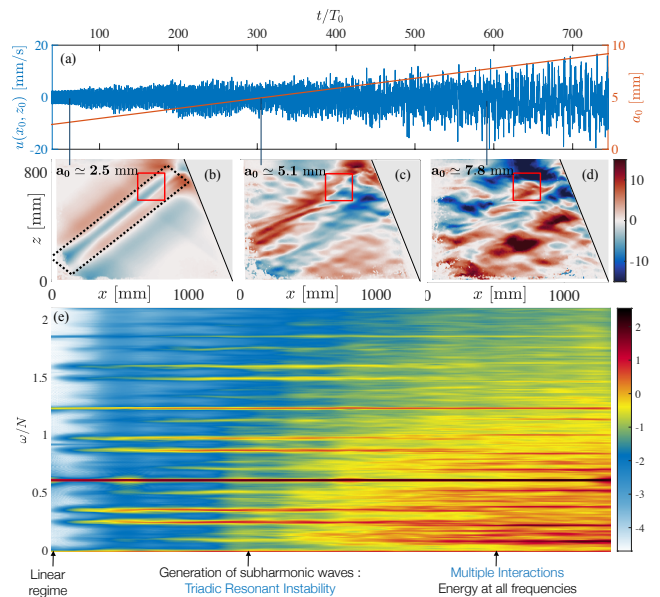


FIG. 3: a) Amplitude ramp (in red) and horizontal velocity component $u(x, z, t)$ measured in a point at the center of the red square shown in (b). b-d) Three snapshots of the horizontal velocity fields (in mm/s) measured when $a = 2.5, 5.1$ and 7.8 mm. e) Time-frequency diagram $S_{\mathbf{u}}(t, \omega)$ of the velocity field of the red square domain (in logarithmic scale). $\alpha = 21.4^\circ$, $L = 1328$ mm, $N = 0.7$ rad/s and $\omega_0/N = 0.62$.

responds to a TRI-perturbed IWA: the two subharmonic waves (around $\omega_-/N = 0.25$ and $\omega_+/N = 0.37$) apparent at this time in Fig. 3(e) clearly satisfy the temporal resonance condition with ω_0 . We also observe $\omega_0 + \omega_-$ and $\omega_0 + \omega_+$, the signatures of the interaction of these subharmonics with the attractor. The third and turbulent-like regime (Fig. 3(d)) is characterized by a broadband Fourier spectrum and a spatial pattern in which no single IWA is evident. When the amplitude is further increased the enrichment of the spectrum is progressive, contrary to numerical simulations of the elastic plates [26]. Although some peaks are still visible at large forcing (especially at the forcing frequency), a continuous spectrum is nonetheless established. We estimate (see Supplemental Material [24]) that the nonlinear interaction between waves typically occurs at a time scale one to ten times larger than the linear one, thus leading to a strong wave turbulent regime.

Spatial Spectra. Figure 4(a) presents the evolution of the wavenumber power spectrum $E_k(k) = k (|\hat{u}(k, \theta, t)|^2 + |\hat{w}(k, \theta, t)|^2)_{\theta,t} / \mathcal{A}$ as the forcing amplitude is gradually increased. Here, $k = |\mathbf{k}|$ is the wavenumber, \mathcal{A} is the area of the trapezoidal domain and \hat{u} and \hat{w} are the Fourier transforms of the components of the velocity field. To improve the signal to noise ratio, the spectrum has been averaged over all angles θ and over many forcing periods, as indicated by $\langle \cdot \rangle_{\theta,t}$. The analysis has been performed only on the low frequency band

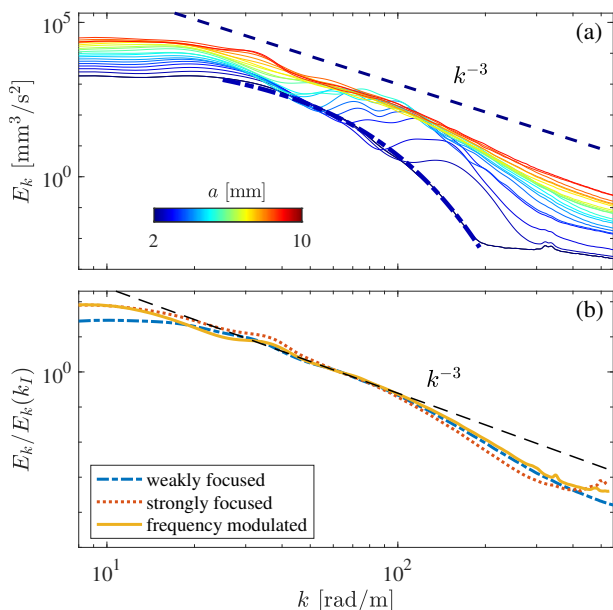


FIG. 4: (a) Power spectral density $E_k(k) = k (|\hat{u}(k, \theta, t)|^2 + |\hat{w}(k, \theta, t)|^2)_{\theta, t} / \mathcal{A}$ as a function of the wavenumber k for the experiment shown in Fig. 3. The spatial Fourier transform of the components of the velocity field \hat{u} and \hat{w} are computed using a hanning window. The different curves correspond to an increase of the amplitude a from 2 to 10 mm (that lasts for 750 periods), with an average over 35 forcing periods for each curve. The thick dash-dotted blue line corresponds to a fit, whose exponential shape is predicted for a linear IWA. (b) Stationary spectrum averaged over 100 periods for different forcings. The different experimental parameters are given in the Supplemental Material [24]. In both panels, the dashed line shows the power law $E_k \simeq k^{-3}$. $k_I \simeq 60$ rad/m is taken in the center of the inertial range.

(*i.e.* $\omega < N$), where propagative waves are predominant (see [27] and Fig. 11 in the Supplemental Material [24]).

In the linear regime, IWAs have been shown to have an exponential power spectrum $E_0 \exp(-\beta k)$, when dissipation due to the lateral walls dominates that of the bulk [20]. This behaviour is indeed observed at small amplitude ($a = 2$ mm), as shown by the dashed blue line. When a is slightly increased, the attractor is destabilized by TRI and a small peak is visible around $k = 150$ rad/m, corresponding to a 4 cm wavelength. Such subharmonic waves have a wavelength smaller than the typical width of the attractor [4]. Further increasing a , the peak not only moves towards smaller values of k but also widens.

This first observation can be explained as the coupling between the spectral energy transfer due to the linear focusing and the one due to nonlinear interactions. The energy focusing is now balanced both by dissipation and by extraction via TRI leading to a wider beam within the IWA. The primary wave, having a larger wavelength, generates secondary waves with larger wavelengths as

well (see Supplemental Material [24]). Moreover, because their group velocity $c_g = N \cos \theta / k$ is larger, subharmonic waves rapidly fill the whole tank.

At large forcing, these different ingredients lead to a richer spectrum that is compatible with a power law decay $E_k \sim k^{-3}$, as shown in Fig. 4(a). The same exponent has been obtained in various numerical simulations with different forcing mechanisms [28, 29].

We have gone on to examine these analyses for experiments with different forcing and geometrical parameters. We have studied a strongly focused IWA that corresponds to a larger Lyapunov exponent than for the weakly focused IWA shown in Fig. 4(a). Taking advantage of the band structure revealed in the kicked attractor experiment, we also forced the stratified fluid via a white noise filtered in the frequency range of the (1,1) attractor shown in Fig. 2(h). In both cases, the exponent -3 is robust as shown in Fig. 4(b).

Conclusion. We have performed the first experimental measurements of internal wave turbulence. The trapezoidal, stably-stratified domain is a robust experimental set-up to study nonlinearly interacting internal waves. Different forcings, whether monochromatic or frequency modulated, lead to a power spectrum with a well-defined power law.

Future work will focus on examination of the frequency spectra. For frequencies below the buoyancy frequency N , one expects a ω^{-2} spectrum similar to the Garrett and Munk spectrum of observed oceanic internal waves [30]. This is often used as a representative statistical description of the internal wave field in studies of nonlinear interaction, despite only an approximate description. For frequencies above N , a steeper ω^{-4} spectrum has been recently reported in numerical simulations [31]. Whether or not both spectra are manifest in experiments remains an open question. To be closer to oceanic circumstances, experiments are being designed with a less constrained geometrical set-up that would allow for three-dimensional dynamics.

Acknowledgements. We are indebted to C. Brouzet, E. Ermanyuk, C. Herbert, L. Maas, L. Saint Raymond and B. Sutherland for useful discussions. This work was supported by the grant ANR-17-CE30-0003 (DisET) and by the LABEX iMUST (ANR-10-LABX-0064) of Université de Lyon, within the program Investissements d’Avenir (ANR-11-IDEX-0007), operated by the French National Research Agency (ANR). This work was supported by a grant from the Simons Foundation (651461, PPC). It has been achieved thanks to the resources of PSMN from ENS de Lyon.

[1] B.R. Sutherland, *Internal Gravity Waves*, Cambridge University Press (2010).

- [2] M.H. Alford *et al.*, *Nature* **521**, 65 (2015).
- [3] M.J. Mercier *et al.*, *Geophys. Res. Lett.* **40**, 5704 (2013).
- [4] T. Dauxois, S. Joubaud, P. Odier, and A. Venaille, *Ann. Rev. of Fluid Mech.* **50**, 131 (2018).
- [5] H. van Haren, *J. of Plankton Res.* **36**, 1124 (2014).
- [6] E.C. Reid *et al.*, *Limnol. Oceanogr.* **64**, 19491965 (2019).
- [7] A. Campagne, B. Gallet, F. Moisy, and P.-P. Cortet, *Phys. Rev. E* **91**, 043016 (2015).
- [8] G.D. Portwood, S.M. de Bruin Kops, and C.P. Caulfield *Phys. Rev. Lett.* **122**, 194504 (2019).
- [9] S. Nazarenko, *Wave Turbulence*, Lecture Notes in Physics **825**, Springer (2011).
- [10] L. Deike, C. Laroche, and E. Falcon, *Europhys. Lett.* **96**, 34004 (2011).
- [11] E. Herbert, N. Mordant, and E. Falcon, *Phys. Rev. Lett.* **105**, 144502 (2010).
- [12] E.A. Kuznetsov, *Journal of Experimental and Theoretical Physics* **93**, 1052 (2001).
- [13] E. Yarom and E. Sharon, *Nature Physics* **10**, 510 (2014).
- [14] B. Miquel, A. Alexakis, C. Josserand, and N. Mordant, *Phys. Rev. Lett.* **111**, 054302 (2013).
- [15] A. Picozzi, J. Garnier, T. Hansson, P. Suret, S. Randoux, G. Millot, D.N. Christodoulides, *Physics Report* **542**, 1 (2014).
- [16] S. Galtier and S.V. Nazarenko, *Phys. Rev. Lett.* **119**, 221101 (2017).
- [17] Y.V. Lvov and E.G. Tabak, *Phys. Rev. Lett.* **87**, 169501 (2001).
- [18] L.R.M. Maas and F.P.A. Lam, *J. Fluid Mech.* **300**, 1–41 (1995).
- [19] G. Pillet, E.V. Ermanyuk, L. Maas, I. Sibgatullin, and T. Dauxois, *J. Fluid Mech.* **845**, 203 (2018).
- [20] F. Beckebanze, C. Brouzet, I.N. Sibgatullin, and L.R.M. Maas, *J. Fluid Mech.* **841**, 614 (2018).
- [21] G. Davis, T. Dauxois, T. Jamin, and S. Joubaud, *J. Fluid Mech.* **880**, 743 (2019).
- [22] H. Scolan, E. Ermanyuk, and T. Dauxois, *Phys. Rev. Lett.* **110**, 234501 (2013).
- [23] L.R.M. Maas, D. Benielli, J. Sommeria, F.P.A. Lam, *Nature* **388**, 557 (1997).
- [24] See Supplemental Material at a web link to be defined later.
- [25] Y. Colin de Verdière and L. Saint Raymond, arXiv:1801.05582v3.
- [26] C. Touzé, S. Bilbao, and O. Cadot, *J. Sound Vib.* **331**, 412 (2012).
- [27] C. Brouzet, E.V. Ermanyuk, S. Joubaud, I. Sibgatullin, T. Dauxois, *Europhysics Letters* **113**, 44001 (2016).
- [28] T. Le Reun, B. Favier, and M. Le Bars, *J. Fluid Mech.* **840**, 498 (2018).
- [29] P. Bouruet-Aubertot, J. Sommeria, and C. Staquet, *Dynamics of Atmospheres and Oceans* **23**, 357 (1996).
- [30] C.J. Garrett and W. Munk, *J. Geophys. Res.* **80**, 291 (1975).
- [31] P. Clark di Leoni and P. D. Mininni, *Physical Review E* **91**, 033015 (2015).
- [32] E. Hopfinger, J.-B. Flor, J.-M., Chomaz, and P. Bonneton, *Exp. Fluids* **11**, 255 (2011).
- [33] B. Voisin, E.V. Ermanyuk, and J.-B. Flor, *J. Fluid Mech.* **666**, 308 (2011).
- [34] C. Brouzet, E. Ermanyuk, S. Joubaud, G. Pillet, and T. Dauxois, *J. Fluid Mech.* **811**, 544 (2017).
- [35] B. Bourget, T. Dauxois, S. Joubaud, and P. Odier, *J. Fluid Mech.* **723**, 1 (2013).
- [36] E. Yarom, A. Salhov, and E. Sharon, *Phys. Rev. Fluids* **2**, 122601(R) (2017).

CASCADE OF RESONANCES TO ACHIEVE INTERNAL WAVE TURBULENCE: SUPPLEMENTARY MATERIAL

Géraldine Davis¹, Timothée Jamin¹, Julie Deleuze¹, Sylvain Joubaud^{1,2}, Thierry Dauxois¹
 1. *Univ Lyon, ENS de Lyon, Univ Claude Bernard, CNRS, Laboratoire de Physique, Lyon, France*
 2. *Institut Universitaire de France (IUF)*

In this supplemental material, we present experimental details, movies, pictures, and additional measurements of the internal wave attractor experiment. Notations are the same as in the above-mentioned paper.

1. Side view of the experimental set-up

A useful experimental technique to visualize internal wave attractors (IWA) is to mark many different isopycnals by a fluorescent dye, which allows us to follow their displacement. This technique has been introduced for the qualitative visualization of lee waves [32], and applied later to the qualitative visualization of stratified wakes and spin-up flows. More recently, this technique has been shown to lead to quantitative measurements using an algorithm to process the experimental dye lines and determine their displacement to sub-pixel accuracy [33].

Figure 5 presents a side view of the experimental tank. Approximately forty horizontal lines are visible from top to bottom. Once the wave generator on the left-hand side of the tank starts to move, internal gravity waves are generated, propagate in the tank, reflect onto the slope, and eventually converge towards an internal wave attractor.

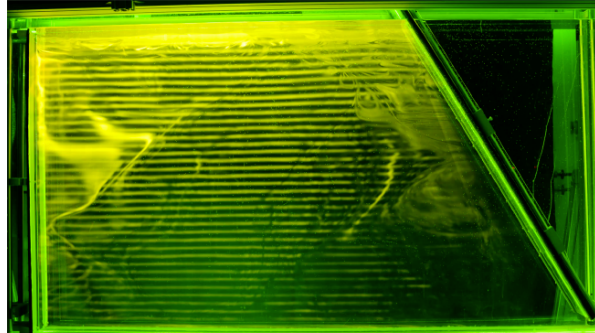


FIG. 5: View of the experimental tank: equidistant isopycnals have been emphasized with rhodamine. $N = 0.77$ rad/s, $\alpha = 29.5^\circ$ and $L = 1600$ mm.

The different movies (sped up by a factor 24) correspond to different experimental parameters:

- Movie1.mp4: (1,1) internal wave attractor obtained with $\omega_0/N = 0.53$ and $a = 2$ mm.
- Movie2.mp4: (1,1) internal wave attractor obtained with $\omega_0/N = 0.53$ and $a = 8$ mm.
- Movie3.mp4: (2,1) internal wave attractor obtained with $\omega_0/N = 0.77$ and $a = 2$ mm.

2. Energy spectrum measurements during the kicked attractor experiment

We compute the energy spectrum of the velocity field for different slope angles to highlight the effect of the tank geometry. These spectra are calculated over the entire duration of the experiment and are displayed in Fig. 6. To

limit the influence of noise, which is more important on the edges of the domain, the integral is performed over an area slightly smaller than the experimental area. The colored regions correspond to the theoretical frequencies of the attractors. The color indicates the type of attractor as mentioned in the caption. One can see that the energy density is indeed larger on these frequency domains.

For the three different cases with a slope, panels (a-c) show the existence of large bumps. On the other hand, for a rectangular tank, panel (d) shows that the resonance frequencies form a discrete set. The non zero width of the peaks is due to dissipation effects.

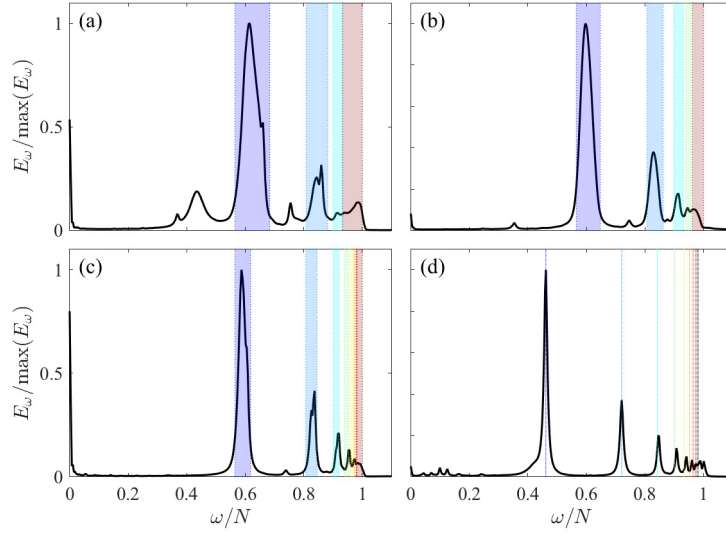


FIG. 6: Normalized energy spectral density computed using the velocity components $u(x, z, t)$ and $w(x, z, t)$ for $t \in [0, 1200]$ s, as in Fig. 2(h). Panels (a), (b), (c) and (d) correspond to $\alpha = 21.4, 15.5, 11.1$ and 0° , with a maximum energy $6.3 \cdot 10^9 \text{ mm}^4$, $1.9 \cdot 10^9 \text{ mm}^4$, $3.1 \cdot 10^9 \text{ mm}^4$ and $6.8 \cdot 10^9 \text{ mm}^4$ respectively. The length of the tank is $L = 1328$ mm, except in (d) where $L = 1750$ mm. Vertical colored bands emphasize the theoretical frequency bands of internal wave attractors in the stationary regime. Purple: attractors (1.1). Dark blue: attractors (2.1). Light blue: attractors (3.1). Green: attractors (4.1). Yellow: attractor (5.1). Orange: attractor (6.1). Red: point attractors. Panel (d) corresponds to the rectangular tank, where the theoretical resonance frequencies form a discrete set.

3. Propagation of secondary waves generated via triadic resonant instability of an IWA

It is known and now reasonably well documented that internal gravity waves are subject to triadic resonant instability (TRI) [4]. Since an internal wave attractor is composed of four different branches that correspond to four internal gravity beams, it is not a surprise to see the destabilization of an IWA, especially of its first branch after focusing (in the upper right part of the tank) where the energy is greatest.

Figure 7 presents the evolution as the forcing amplitude a increases of the horizontal velocity field filtered around $\omega_+/N = 0.37$ (*i.e.* around one of the two secondary-wave frequencies) when the tank is forced at $\omega_0/N = 0.62$. For the smallest forcing amplitude, as shown by panel (a), the field is intense only on the upper part of the tank, close to the first branch, and the pattern has a typical wavelength $\lambda \simeq 50$ mm. Then, after successive reflections, the beam fills the entire tank (panel b). We can see that this phenomenon is accompanied by a gradual increase in wavelength, which reaches about 130 mm in panels (c) and (d).

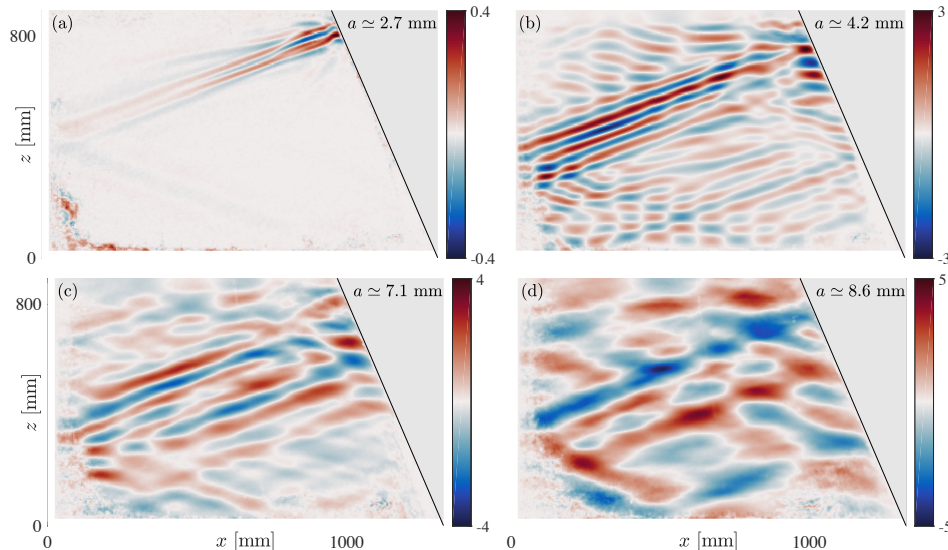


FIG. 7: Different instantaneous horizontal velocity fields (in mm/s), filtered around the subharmonic frequency $\omega_+/N = 0.37$.

Figure 8 presents quantitative measurements to support this observation. Panel (a) shows the wavelength λ_0 of the second branch of the attractor over time. This wavelength has been defined as the wavelength associated to the average wave vector $\langle k_0 \rangle$, weighted by the power spectral density $E_{\mathbf{k}}$

$$\lambda_0 \equiv \frac{2\pi}{\langle k_0 \rangle} \quad \text{with} \quad \langle k_0 \rangle \equiv \frac{\int d\mathbf{k} |\mathbf{k}| E_{\mathbf{k}}(\mathbf{k}, \omega_0)}{\int d\mathbf{k} E_{\mathbf{k}}(\mathbf{k}, \omega_0)}, \quad (1)$$

where $E_{\mathbf{k}}(\mathbf{k}, \omega_0)$ is computed from the velocity field filtered at the forcing frequency ω_0 , and the integrals over \mathbf{k} are computed only for $k_x < 0, k_z > 0$ (which corresponds to the second branch of the attractor). We see a 50% increase of this wavelength, between the beginning and the end of the experiment, since λ_0 rises from approximately 250 to 380 mm. In the same way, we can compute the characteristic wavelength λ_+ of the secondary wave presented in Fig. 7 using Eq. (1), where the velocity field is filtered around $\omega_+/N = 0.37$. This increase of the wavelength of the primary wave is clearly correlated with an increase of the wavelength of the considered secondary wave, as shown in panel 8(b): the latter doubles between the beginning and the end of the experiment. As the group velocity of a wave is proportional to its wavelength, it also doubles from 8 to 16 mm/s. The distance travelled during the characteristic dissipation time (of the order of 150 s) thus increases from 1 to 2 m. The beam can interfere with itself and possibly present a quasi-stationary structure.

We just saw that in larger forcing cases (Fig. 8), the attractor is thicker and the secondary wavelength is larger: consequently, the secondary waves fill available space and sometimes look like standing waves. A weakly focused attractor would moreover favor this effect since it already has a longer wavelength in the linear regime. The quasi-stationarity of the secondary waves is thus related to the wavelength of the attractor. This interpretation is different from the one suggested in [34], which described it as a consequence of the quasi-stationarity of the attractor.

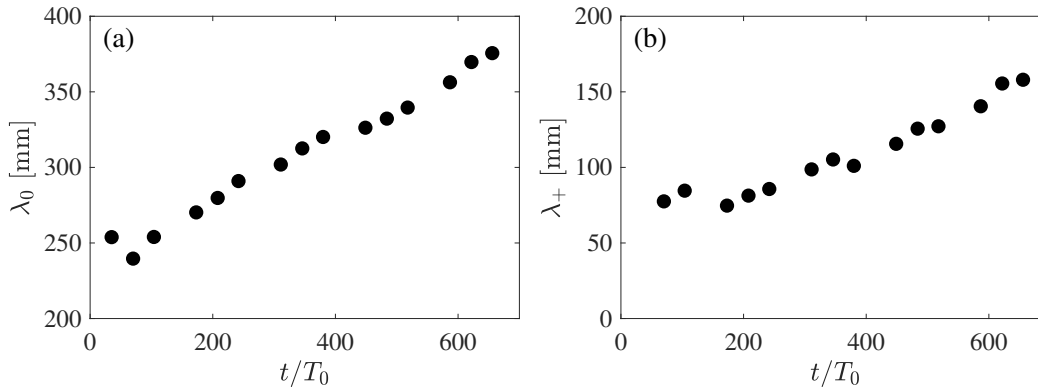


FIG. 8: Evolution of the dominant wavelength of the attractor for a forcing frequency $\omega_0/N = 0.62$ (a) and of one of the corresponding subharmonic wave with a frequency close to $\omega_+/N = 0.37$ (b).

4. Experimental parameters

Table I gives the experimental parameters used for the different stationary spectrum shown in Fig. 4(b). For the frequency modulated forcing, the amplitude signal is given in Fig. 9 and is characterized by its standard deviation.

Forcing	Wave period T_0 (s)	Amplitude a (mm)	angle α ($^\circ$)	L (mm)
weakly focused	14.5	growth from 8.3 mm to 9.4 mm	21.4	1328
strongly focused	13.6	14	25.3	1455
frequency modulated	[12.9 - 14.9]	$\langle a^2 \rangle^{1/2} = 7$ mm	15.7	1340

TABLE I: Experimental parameters for Fig. 4(b)

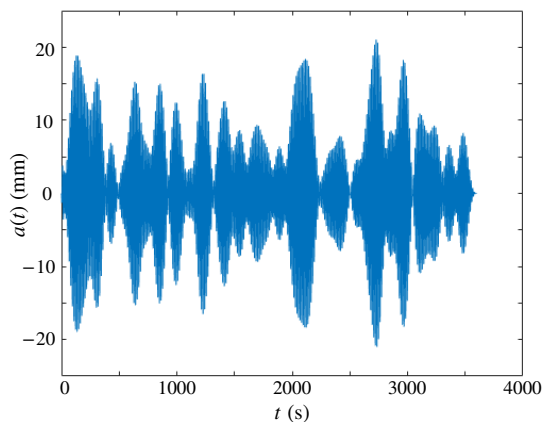


FIG. 9: Amplitude signal used for the frequency modulated forcing.

5. Nonlinear time scale

The wave turbulence theory is developed within a framework of weak turbulence, where nonlinear interactions

induce wave modulation with a typical time scale – called the nonlinear time scale and denoted τ_{NL} – that has to be long enough compared to the wave period $T = 2\pi/\omega$.

Let us consider the simple case of a weakly resonant interaction between three monochromatic plane waves i , j and ℓ . Assuming that the wave amplitudes vary slowly with respect to the periods of the waves, straightforward calculations [4, 35] lead, at first order, to three amplitude equations for the stream functions similar to

$$\frac{d\psi_\ell}{dt} = I_\ell \psi_i \psi_j - \frac{\nu}{2} k_\ell^2 \psi_\ell, \quad (2)$$

where I_ℓ is a function of the characteristics of the triad (i, j, ℓ) in interaction. The viscous time scale $\tau_\nu \approx 1/(\nu k_\ell^2) \in [100; 2500]$ s can be immediately deduced from Eq. (2).

On the one hand, these equations lead to triadic resonance *instability* when the amplitude of one wave is large enough to generate two other ones (with a viscous threshold, see [4, 35]). On the other hand, without any threshold, two waves can lead to the growth of a third wave corresponding to triadic *interaction* (which comes directly from Eq. (2) by considering ψ_i and ψ_j constant). These nonlinear mechanisms come with timescales that we estimate experimentally.

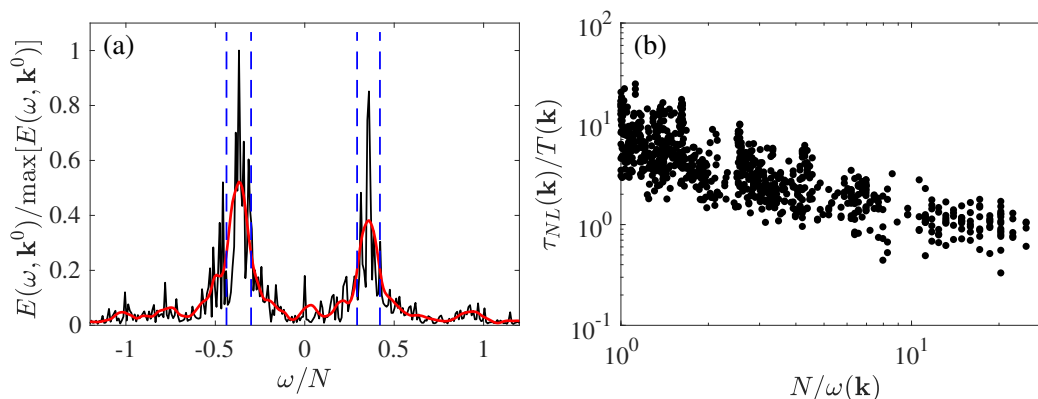


FIG. 10: (a) Temporal Fourier spectrum taken from the power spectrum $E(\omega, \mathbf{k})$ for the given wavevector $(k_x^0, k_z^0) = (-0.15, 0.63)$ rad/m (thin black lines). The thick red curve is a smoothed curve. The dashed vertical lines indicate the width at mid-depth of each peak. (b) Experimental normalized nonlinear time τ_{NL} given by the width at mid-depth of the peaks from (a)-like spectra as a function of the normalized wave frequency.

As recently shown by Yarom, Salhov and Sharon [36], the nonlinear time scale is related to the width of peaks in temporal spectra, as the one represented in Fig. 10(a), taken from the power spectrum at a given wavevector \mathbf{k}^0 . The nonlinear time associated to this wavevector is then defined by $\tau_{NL} = 2\pi/\Delta\omega$, where $\Delta\omega$ is the mean width at mid-depth of the two peaks around $\omega = \pm N \sin \theta_{\mathbf{k}^0}$. The ratio between the nonlinear and the linear times is then represented in Fig. 10(b) for various wavevectors in the inertial range ($k \in [20; 100]$ rad/m, see Fig. 4). A large majority of the values for τ_{NL}/T are lying between 1 and 10. This order of magnitude does not correspond to the theoretical framework of *weak* wave turbulence ($\tau_{NL}/T \gg 1$). Nevertheless, as shown by Fig. 11 displaying the normalized power spectra as a function of θ and ω , the energy is localized around the dispersion relation of internal waves (dashed lines) for all cases. This confirms we actually observe multiple internal wave interactions leading to wave turbulence.

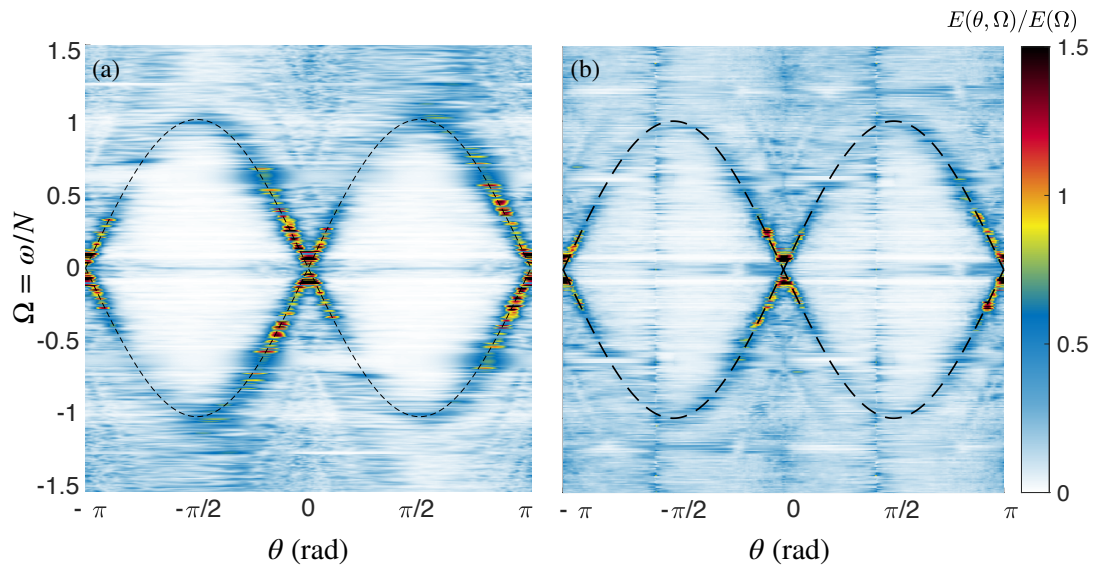


FIG. 11: Normalized power spectrum $E(\theta, \omega)/(\int_0^{2\pi} E(\theta, \omega)d\theta)$ for (a) the weakly focused case and (b) the frequency modulated case. Dashed lines correspond to the dispersion relation of internal waves $\omega/N = \sin \theta$.